Combustion Theory and Modelling
Vol. 16, No. 5, 2012, 774–798

Simulations of normal and inverse laminar diffusion flames under oxygen enhancement and gravity variation

P. Bhatia[a*], V. R. Katta[b], S. S. Krishnan[c], Y. Zheng[d], P. B. Sunderland[e] and J. P. Gore[d]

[a]*Mechanical and Automobile Engineering Department, ITM University, Gurgaon 122017, India;* [b]*Innovative Scientific Solutions, Inc., Dayton, OH 45440, USA;* [c]*Department of Mechanical Engineering, Purdue School of Engineering and Technology, IUPUI, Indianapolis, IN 46202, USA;* [d]*School of Mechanical Engineering, Purdue University, West Lafayette, IN 47907, USA;* [e]*Department of Fire Protection Engineering, University of Maryland, MD 20742, USA*

(*Received 21 July 2011; final version received 12 January 2012*)

Steady-state global chemistry calculations for 20 different flames were carried out using an axisymmetric Computational Fluid Dynamics (CFD) code. Computational results for 16 flames were compared with flame images obtained at the NASA Glenn Research Center. The experimental flame data for these 16 flames were taken from Sunderland *et al.* [4] which included normal and inverse diffusion flames of ethane with varying oxidiser compositions (21, 30, 50, 100% O_2 mole fraction in N_2) stabilised on a 5.5 mm diameter burner. The test conditions of this reference resulted in highly convective inverse diffusion flames (Froude numbers of the order of 10) and buoyant normal diffusion flames (Froude numbers ∼0.1). Additionally, six flames were simulated to study the effect of oxygen enhancement on normal diffusion flames. The enhancement in oxygen resulted in increased flame temperatures and the presence of gravity led to increased gas velocities. The effect of gravity-variation and oxygen enhancement on flame shape and size of normal diffusion flames was far more pronounced than for inverse diffusion flames. For normal-diffusion flames, their flame-lengths decreased (1 to 2 times) and flames-widths increased (2 to 3 times) when going from earth-gravity to microgravity, and flame height decreased by five times when going from air to a pure oxygen environment.

Keywords: microgravity; diffusion flames; ethane; global; steady state

Nomenclature

0g_IDFxx	Inverse diffusion flame under microgravity with oxidiser composed, respectively, of xx and (100 - xx) mole% of O_2 and N_2.
0g_NDFxx	Normal diffusion flame under microgravity with oxidiser composed, respectively, of xx and (100 - xx) mole% of O_2 and N_2.
1g_IDFxx	Inverse diffusion flame under earth-gravity with oxidiser composed, respectively, of xx and (100 - xx) mole% of O_2 and N_2.
1g_NDFxx	Normal diffusion flame under earth-gravity with oxidiser composed, respectively, of xx and (100 - xx) mole% of O_2 and N_2.
υ	Kinetic viscosity.
D	Burner inner diameter.

*Corresponding author. Email: pramodbhatia77@gmail.com

ISSN: 1364-7830 print / 1741-3559 online

http://dx.doi.org/10.1080/13647830.2012.658440
http://www.tandfonline.com

f	Mixture Fraction (Fraction of mass contributed by fuel, obtained by post-processing the computational results).
Fr	Froude Number ($= \frac{v_0^2}{g.D}$).
g	Acceleration due to gravity at earth's surface ($= 9.80665$ m/s).
$L_{f,\,comp}$	Computed flame length.
$L_{f,\,exp}$	Measured flame length.
$\dot{Q}$	Heat release rate for complete combustion using lower heating value of fuel.
r	Radial distance from the axis of burner.
Re	Reynolds number ($= \frac{u_0.d}{\upsilon}$).
T	Temperature.
$T_{ad,\,d}$	Adiabatic flame temperature calculated using chemical equilibrium analyses (CEA) for 2000 species.
$T_{ad,\,g}$	Adiabatic flame temperature calculated using complete reaction with one step global chemistry.
T_{max}	Maximum computed flame temperature.
v	Axial velocity.
v_0	Jet velocity.
v_b	Axial velocity contribution due to buoyancy.
v_{co}	Co-flow velocity.
w_{comp}	Computed flame width.
w_{exp}	Experimental flame width.
Y_i	Mass fraction of species *i*.
$X_{O_2,\infty}$	Mole fraction of O_2 in the jet inflow.
z	Axial distance from the burner tip.

1. Introduction and scope of work

Laminar jet diffusion flames are fundamental to combustion. Their study has contributed to myriad advances in combustion science, including the development of theoretical, computational, and diagnostic combustion tools. Laminar jet flames are also pertinent to the turbulent flames of more practical interest.

It is possible to study these flames in two different configurations –

(i) Oxygen enriched jet issues into fuel and forms an inverse diffusion flame configuration, and
(ii) Fuel jet encounters an oxygen enriched environment and forms a normal diffusion flame configuration.

Both these configurations have been of great interest for the past few decades, and they can arise on earth [1] and in space. While past studies and current tests have focused more on normal diffusion flames (NDF), the inverse diffusion flame (IDF) configuration is also of importance to possible fire scenarios on board the space station or extra-vehicular activity (EVA) type environments (where a high velocity high oxygen jet may encounter fuel) [2].

Recently, spacecraft fire safety has been a matter of concern. For example, a few years ago in 1997 there was an accidental fire on the Mir space station which threatened the lives of its six crew members. This fire [3] involved an oxygen jet leaking from a lithium-perchlorate oxygen generator and involved three factors not normally encountered in terrestrial fires: enhanced oxygen, inverse flames and microgravity.

Some of the benefits of oxygen enhanced combustion include increased thermal efficiency, peak temperature and stability, reduced combustor size and potentially reduced pollutant emissions. The reduction in cost of the oxygen separating devices has also contributed to the success of oxygen-enhanced combustion [1].

Oxygen enrichment and gravity variation can have a significant effect on the flame properties. For example, 2000 species CEA (chemical equilibrium analysis) calculations show that the adiabatic flame temperature for ethane increases from 2258 K in air to 3082 K in oxygen, i.e., an increase of about 37% in the presence of oxygen compared to air [4]. Laminar jet diffusion flames were one of the first flame configurations to be observed in microgravity ([5] and references therein) and such flames were reported to be longer than buoyant flames [6]. This [5] and subsequent studies [7,8] were mostly confined to measurements of luminous flame shapes for normal diffusion flames. Bahadori and co-workers considered microgravity methane and propane gas jet flames burning in various pressure ambients of 15−50% O_2 in N_2 [8]. They noted that increased oxygen concentrations led to shorter flames and increased soot concentrations.

Sunderland and co-workers studied pure oxygen ethylene diffusion flames in normal and inverse spherical configurations [9]. However, they used diluted fuel and their objective was to study flame structure and hydrodynamic effects under microgravity conditions. Studies by Van-Hulle and co-workers also involved pure oxygen; however, they studied turbulent methane diffusion flames [10].

Recent work by Blevins and co-workers considered laminar ethylene/air inverse diffusion flames for soot structure and chemical analysis in earth-gravity [11]. Shaddix and co-workers investigated steady and pulsed normal and inverse jet diffusion flames of methane/air and ethylene/air stabilised on a slot burner [12].

Also, Laminar Soot Processes (LSP) space experiments summarised in refs. [13,14] considered non-buoyant ethylene and propane laminar jet diffusion flames burning in air. These studies support the belief that microgravity fires pose extraordinary fire safety risks due to increased soot emission and longer flame length. Hwang and Gore experimentally determined the total infrared radiation heat flux, spectral radiation intensities and soot concentration in various oxygen enriched conditions. However, their study was limited to earth-gravity methane diffusion flame configurations [15].

While many experimental studies have been conducted in the past, in recent times there has been extensive effort to computationally understand flame behaviour [16–26]. A summary of these references is discussed later. Simulations provide greater insight and far more physical information from the results, and in some cases computations are easier to perform. However, because of their large resource requirements, computer simulation for flames is a challenging task. Experiments on the other hand have safety issues involved in the use of high oxygen concentrations. Additionally, microgravity experiments are comparatively more difficult to perform than earth-gravity experiments. Hence, unfortunately, because of genuine constraints, systematic studies of jet flames with oxygen enrichment beyond 50% have not been performed. This is especially true for microgravity conditions and for inverse configuration.

Inverse flames have mixture-fraction/temperature/time trajectories for soot processes that are entirely different from those of normal flames. Inverse flames can be used to examine phenomena that are obscured in normal flames. Sidebotham and Glassman [27] noted that inverse flames facilitated the study of soot formation because soot oxidation was generally absent from these flames. Kaplan and Kailasanath [28] examined soot formation in inverse diffusion flames using a detailed numerical model. Blevins *et al*. [29] found that inverse flames facilitated the collection of soot precursors and early soot. Sunderland *et al*. [9] used

inverse spherical flames to distinguish the effects of convection direction and stoichiometry on soot formation. Past work on microgravity laminar jet diffusion flames emphasised normal flames burning in air. Many of these studies focused on flame appearance and correlations of flame shape [6,7,14,30]. Measurements using advanced diagnostics were provided by, for example, the space experiments of Ref. [13] and the ground-based studies of Refs. [31,32]. Absent from this past work are observations of flames similar to the Mir fire – namely oxygen-enhanced, inverse gas-jet diffusion flames in microgravity.

The present study is motivated by the above considerations and by the fundamental interest of the combustion community to understand flame behaviour. The present work's objectives are to understand and predict flame behaviour under:

(a) Microgravity (μ-g) and earth-gravity environments,

(b) Oxygen enrichment, and

(c) Normal and inverse diffusion flame configurations.

Steady-state calculations have been performed for global chemistry (5 species and 1 reaction) using the axisymmetric computational tool developed by Katta *et al.* [17−19]. Detailed chemistry [33], soot chemistry [34−36], and a modified optically thin model for radiation [26] implemented by Katta will be incorporated in the future studies. Ethane fuel (1.0 mole fraction) was used to examine the effects of oxygen enhancement (0.21, 0.3, 0.5 and 1.0 mole fraction) in nitrogen. Table 1 presents the test conditions.

The flame lengths and widths from the computations are calculated based on the following definitions: Flame length was defined as the distance between the burner tip and the location of the peak temperature along the centreline. Flame width was defined as twice the maximum radial distance of the maximum temperature location from the centreline.

Table 1. Test conditions for the computed cases.

CASES	GRAVITY	DIFFUSION	O_2 MOLE FRACTION	V_0 (mm/s)	Fr	Re	$\dot{Q}$(W)
CASE 1 [1g_IDF21]	1-g	Inverse	0.21	866	13.9	312	72
CASE 2 [1g_IDF30]	1-g	Inverse	0.3	866	13.9	310	102
CASE 3 [1g_IDF50]	1-g	Inverse	0.5	866	13.9	310	171
CASE 4 [1g_IDF100]	1-g	Inverse	1.0	866	13.9	311	342
CASE 5 [0g_IDF21]	0-g	Inverse	0.21	866	∞	312	72
CASE 6 [0g_IDF30]	0-g	Inverse	0.3	866	∞	310	102
CASE 7 [0g_IDF50]	0-g	Inverse	0.5	866	∞	310	171
CASE 8 [0g_IDF100]	0-g	Inverse	1.0	866	∞	311	342
CASE 9 [1g_NDF21]	1-g	Normal	0.21	52	0.05	39	72
CASE 10 [1g_NDF30]	1-g	Normal	0.3	74	0.1	55	102
CASE 11 [1g_NDF50]	1-g	Normal	0.5	124	0.28	92	171
CASE 12 [0g_NDF21]	0-g	Normal	0.21	52	∞	39	72
CASE 13 [0g_NDF30]	0-g	Normal	0.3	74	∞	55	102
CASE 14 [0g_NDF50]	0-g	Normal	0.5	124	∞	92	171
CASE 15 [1g_NDF30]	1-g	Normal	0.3	52	0.05	39	72
CASE 16 [1g_NDF50]	1-g	Normal	0.5	52	0.05	39	72
CASE 17 [1g_NDF100]	1-g	Normal	1.0	52	0.05	39	72
CASE 18 [0g_NDF30]	0-g	Normal	0.3	52	∞	39	72
CASE 19 [0g_NDF50]	0-g	Normal	0.5	52	∞	39	72
CASE 20 [0g_NDF100]	0-g	Normal	1.0	52	∞	39	72

The experimental flame lengths and flame widths were obtained from Ref. [4]. Where blue contours were identifiable, stoichiometric flame lengths were measured from the burner tip to the farthest point of blue emission. Alternatively, luminosity lengths were measured to the end of the yellow region on the flame centreline. Flame widths were found from the widest parts of the blue or yellow regions. The values of flame lengths and widths are presented in Table 2.

2. Mathematical Model

The axisymmetric mathematical tool known as UNICORN (Unsteady Ignition and Combustion using ReactioNs) [17,18] is used to simulate the steady jet inverse diffusion flames considered in this study. It solves for continuity, axial- and radial-momentum, and enthalpy and species conservation equations on a staggered grid system. Using cylindrical coordinates, these equations can be written in the following general form:

$$\frac{\partial(\rho)}{\partial t} + \frac{1}{r}\frac{\partial(r\rho u)}{\partial r} + \frac{\partial(\rho v)}{\partial z} = 0 \tag{1}$$

$$\frac{\partial(\rho\Phi)}{\partial t} + \frac{\partial(\rho u\Phi)}{\partial r} + \frac{\partial(\rho v\Phi)}{\partial z} = \frac{\partial}{\partial r}\left(\Gamma^{\Phi}\frac{\partial\Phi}{\partial r}\right) + \frac{\partial}{\partial z}\left(\Gamma^{\Phi}\frac{\partial\Phi}{\partial z}\right) - \frac{\rho u\Phi}{r} + \frac{\Gamma^{\Phi}}{r}\frac{\partial\Phi}{\partial r} + S^{\Phi} \tag{2}$$

Here ρ is density, t is time, and u and v, respectively, represent the radial (r) and axial (z) velocity components. The equations represented by this general form depend on the choice of Φ. The transport coefficient Γ^{Φ} and source term S^{Φ} appearing in the above equation are provided in Table 1 of Ref. [20] (also described in Ref. [21]). Replacing Φ in Equation (2) by u, v, enthalpy and species mass fraction will respectively give us radial- and axial-momentum equations, and enthalpy and species conservation equations. The transport coefficient Γ^{Φ} becomes viscosity for momentum equations, thermal conductivity divided by specific heat for the enthalpy equation and ρ multiplied by effective species diffusion coefficient for the species conservation equation. Introducing the global species conservation equation and the perfect gas state equation completes the equations. Time marching is used to achieve steady-state.

The body force term due to the gravitational field is included in the axial momentum equation source term. A clustered mesh system is employed for these computations to trace the large gradients near the flame surface. The five species involved in the global chemistry calculations are: Ethane (C_2H_6), Oxygen (O_2), Nitrogen (N_2), Water (H_2O) and Carbon dioxide (CO_2).

Enthalpy, viscosity, thermal conductivity, and binary molecular diffusion of all the species are calculated from polynomial curve fits developed for the temperature range 300–5000 K. Mixture viscosity and thermal conductivity are then estimated using the Wilke and Kee expressions, respectively. Molecular diffusion is assumed to be of the binary diffusion type, and the diffusion velocity of species is calculated using Fick's law and the effective diffusion coefficient of that species in the mixture [37].

The finite-difference forms of the momentum equations are obtained using an implicit QUICKEST scheme [38], and those of the species and energy equations are obtained using a hybrid scheme of upwind and central differencing. The pressure field is calculated by simultaneously solving the discrete form of the pressure Poisson equation at all the grids and using the LU (Lower and Upper diagonal) matrix decomposition technique. The boundary

Table 2. Experimental and computational flame lengths and flame widths. Maximum and adiabatic temperatures.

CASES	$L_{f,\,comp}$ (mm) Global Chemistry [Based on Temperature]	$L_{f,\,exp}$ (mm) ** [4]	W_{comp} (mm) Global Chemistry [Based on Temperature]	W_{exp} (mm)** [4]	T_{max} (K) Global Chemistry	$T_{ad,\,g}$ (K) GLOBAL CALCULATIONS; 5 SPECIES	$T_{ad,\,d}$ (K) CEA CALCULATIONS 2000 SPECIES
CASE 1 [1g_IDF21]	15.1	14	5.0	5.9	2170	2382	2250
CASE 2 [1g_IDF30]	15.1	13	5.2	6.0	2650	2977	2553
CASE 3 [1g_IDF50]	15.3	14	6.0	6.7	3440	3981	2839
CASE 4 [1g_IDF100]	18.5	17	7.6	9.0	4520	5491	3082
CASE 5 [0g_IDF21]	15.8	16	5.0	6.0	2170	2382	2250
CASE 6 [0g_IDF30]	15.8	14	5.4	6.4	2640	2977	2553
CASE 7 [0g_IDF50]	16.5	15	6.4	7.4	3450	3981	2839
CASE 8 [0g_IDF100]	20	19	9	11	4480	5491	3082
CASE 9 [1g_NDF21]	25	25	8.8	8.1	2220	2382	2250
CASE 10 [1g_NDF30]	20.6	18	9.0	8.1	2790	2977	2553
CASE 11 [1g_NDF50]	20.2	16	9.4	7.7	3690	3981	2839
CASE 11 [0g_NDF21]	17.4	21	24.1	26	2170	2382	2250
CASE 12 [0g_NDF30]	18.6	24	24.1	28	2730	2977	2553
CASE 13 [0g_NDF50]	20.2	32	20.6	24	3620	3981	2839
CASE 15 [1g_NDF30]	20	–	8.6	–	2790	2977	2553
CASE 16 [1g_NDF50]	10.7	–	7.8	–	3600	3981	2839
CASE 17 [1g_NDF100]	4.3	–	6.0	–	4310	5491	3082
CASE 18 [0g_NDF30]	15.1	–	20.8	–	2660	2977	2553
CASE 19 [0g_NDF50]	9.1	–	13.4	–	3400	3981	2839
CASE 20 [0g_NDF100]	4.3	–	7.4	–	4100	5491	3082

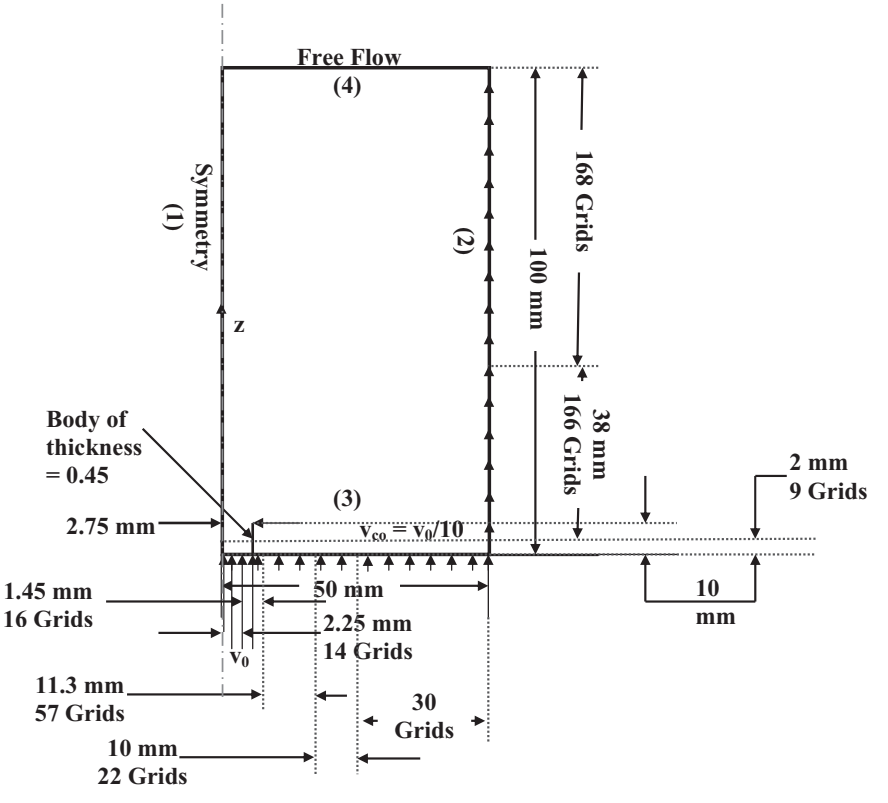

Figure 1. Computational domain, boundary conditions, burner dimensions and grid distribution.

conditions are treated in the same way as that reported in an earlier paper [23]. As shown in Figure 1, flat velocity profiles are used at the fuel and oxidise inflow (boundary 3). The free flow condition is used at outflow (boundary 4). For this purpose a simple extrapolation procedure with weighted zero- and first-order terms was used to estimate the flow variables on the outflow boundary. A constant velocity condition is imposed at the outer boundary and this velocity is identical to the co-flow velocity (boundary 2). The arrows on boundaries 2 and 3 represent the velocity direction. The inner boundary which passes through the axis of symmetry is treated accordingly (boundary 1).

UNICORN has been extensively validated in the past by simulating various steady and unsteady counterflow [25] and co-flow [23,25,26] jet diffusion flames and by comparing the results with experimental data. This gives confidence that UNICORN can accurately simulate the structure of flames.

3. Grid and domain optimisation

The present simulations involved a round 5.5 mm diameter burner and quiescent ambient gas at 0.98 bar and 298 K. Figure 1 presents the geometry of the axisymmetric computational domain. The computational domain extends 100 mm and 50 mm in the axial (z) and radial (r) directions, respectively, and is represented by a staggered, clustered 343 × 139 grid system. The co-flow velocity is set at 1/10th of the jet velocity. The effect of the round 5.5 mm

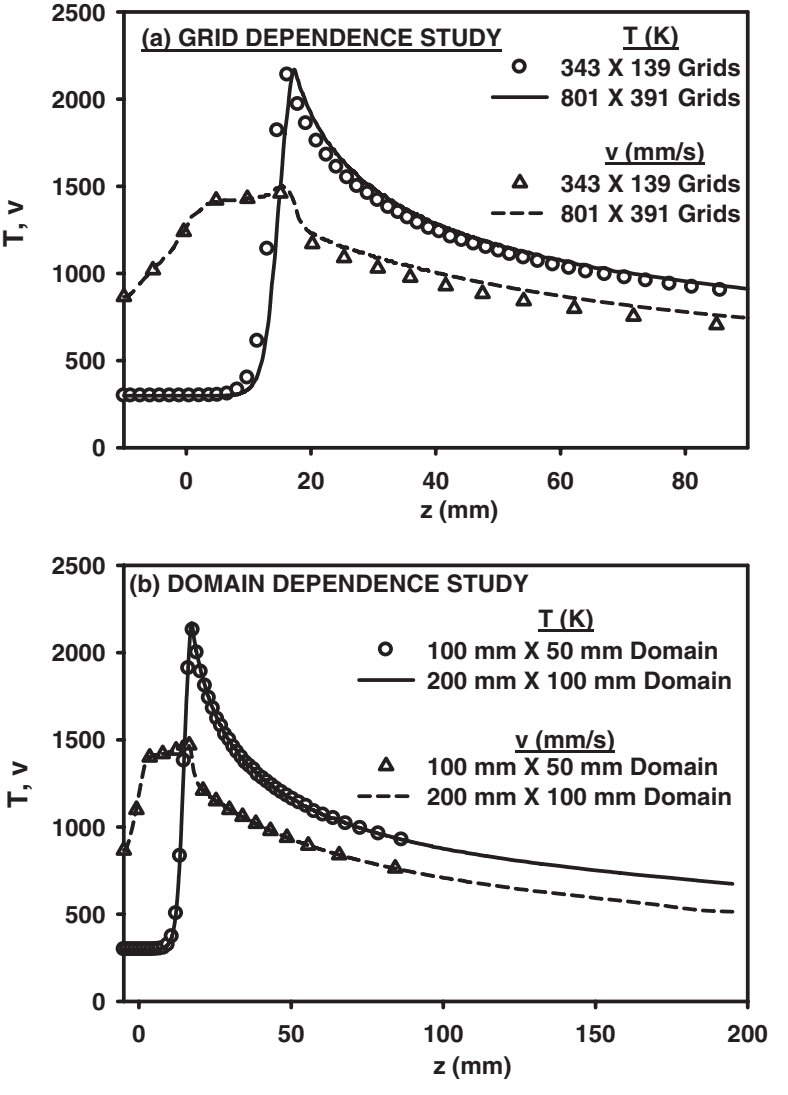

Figure 2. (a) Grid dependence study for 0g_IDF21. The two grid sizes considered are: 801 × 391 and 343 × 139. (b) Domain dependence study for 0g_IDF21. The two domains considered are: 200 mm × 100 mm and 100 mm × 50 mm.

diameter burner on flow dynamics is modelled by including an adiabatic rectangular body of thickness 0.45 mm inside the computational domain. The body height is 10 mm (Table 1).

The grid sensitivity study was performed (to obtain grid independence) and is illustrated here for the example case of 0g_IDF21. The domain size was kept identical and the grid spacing (both in z and r directions) was reduced to less than half. Hence the grid size was increased from 343 × 139 to 801 × 391. Figure 2(a) presents reasonable agreement between centreline axial velocities and temperatures. Identical peak temperature (2170 K) is predicted by both computations. However approximately 3% and 4% differences in flame lengths and peak velocities were, respectively, observed between the two computations. Considering that the total number of cells were increased by about seven times, these

differences are considered acceptable and the computational results can be considered grid independent.

In the actual experiment [4] there was no enforced co-flow and the burner was made of stainless-steel with a knife-edge tip. The burner was much longer in length. Precise simulation for the experimental setup would require a very large computational domain. This was impractical and hence some engineering approximations have been made while performing the computations. The assumptions of specified co-flow velocity, boundary temperatures and other boundary conditions are deviations from the actual experiments. Hence, it becomes vital that the domain effects should be studied and domain independence should be obtained. The domain independence was obtained and is demonstrated here for the example case of 0g_IDF21. Computations were performed for 200 mm $\times$ 100 mm domain and the results were compared with 100 mm $\times$ 50 mm domain. The grid spacing was kept identical for the overlapping region of the two cases. Figure 2(b) shows the comparisons between the velocity and temperature profiles for the two domains studied. There is very little difference between these two results, therefore, the computational results are considered domain independent. In addition we also increased the co-flow from $1/10^{\text{th}}$ to 1/5th of the jet velocity and found that there was no visible difference in the results. Burner length was also decreased from 10 mm to 5 mm. Although the exit velocity from the burner exit differed slightly for the two cases, we found that it did not affect our downstream results and conclusions.

4. Results and discussion

Table 1 presents the test conditions for the 20 cases computed using global chemistry. A detailed discussion of the results is presented in the following section. The flame images from Ref. [4] and temperature (K) contours from the present computations were compared for all the computed cases. The comparisons could only be qualitative because of the differences in the quantities being displayed as well as the differences between the boundary conditions in the experiments and the computations. Comparisons showed remarkable qualitative similarities between the shapes and locations of colour changes observed in the flame photographs and contour changes observed in the calculated temperature contour plots. We must mention that for some cases the flame appears to be dim at certain locations where temperatures can still be high. This is because cameras have limitations and hence can only capture the luminous emission if it is above certain minimum luminosity. It is expected that including radiation and detailed chemistry in the computational model is likely to yield better agreement with the experiments. The local deceleration immediately following the flame tip (for earth-gravity flames [Figure 3]) and the presence of downward pressure forces observed for some cases discussed in the computational results could not be verified experimentally due to the small length scales at which these occur. Plots also indicated that the axial component is prominent in the earth-gravity flames.

The difference between adiabatic equilibrium temperature and the maximum temperature increased significantly with oxygen enhancement. The computed maximum temperatures are much higher than the adiabatic equilibrium temperatures calculated from equilibrium reactions containing 2000 species. This is caused by the current assumption of the limitations of global chemistry which is far from any real chemistry.

4.1 *General observations – axial velocity and temperature*

Figures 3 and 4 show the computed axial velocity and temperature at the centreline as a function of axial location (z). Figures 3(a) and 4(a) show the results for the inverse diffusion

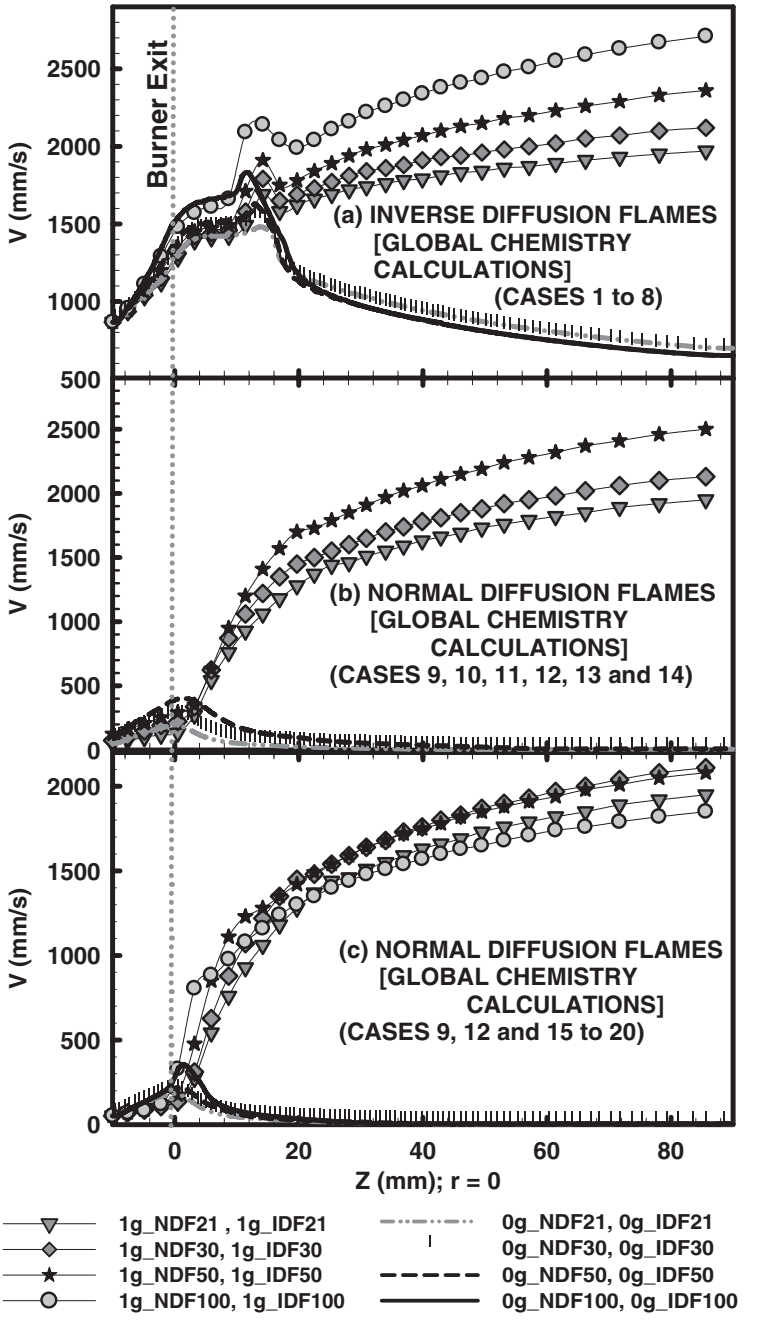

Figure 3. Comparisons of axial velocities (v) at the centreline (r = 0.0) for: (a) Inverse Diffusion Flames [cases 1 to 8], (b) Normal Diffusion Flames [cases 9 to 14] and (c) Normal Diffusion Flames [cases 9, 12 and 15 to 20].

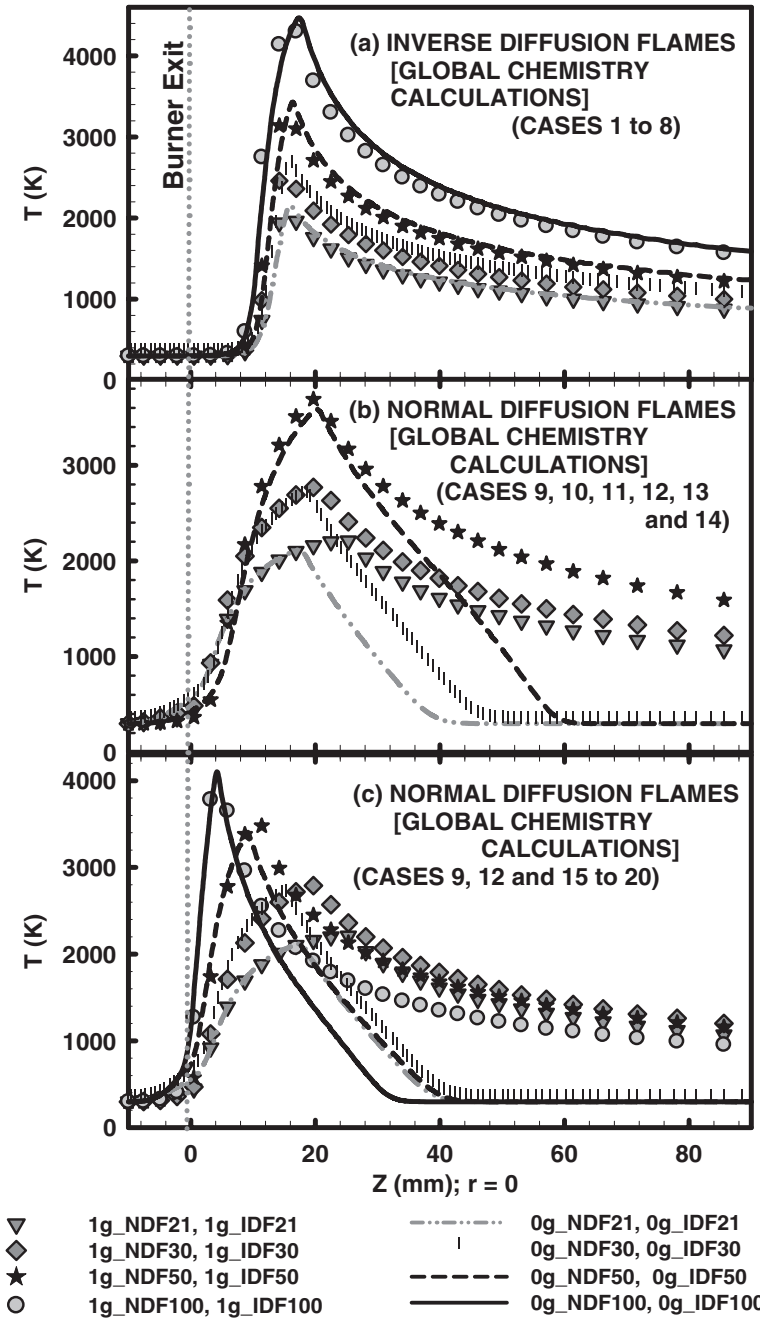

Figure 4. Comparison of temperatures at the centreline (r = 0.0) for: (a) Inverse Diffusion Flames (cases 1 to 8), (b) Normal Diffusion Flames [cases 9 to 14] and (c) Normal Diffusion Flames [cases 9, 12 and 15 to 20].

flames. Figures 3(b), 3(c), 4(b) and 4 (c) show the results for the normal diffusion flames. All the axial velocity plots show acceleration due to thermal expansion in the high temperature zone followed by a slight deceleration. These plots also indicate continued acceleration due to buoyancy in the earth-gravity flames beyond the flame tip (location of maximum temperature on the centreline) and the deceleration due to shear forces for the microgravity flames. These trends are supported by Refs. [8] and [39].

The temperature plots show the increase in temperature in the reaction-diffusion zone where there is buoyant acceleration and indicate a broadened high temperature zone in the case of the normal diffusion flames as compared to the inverse diffusion flames (with identical heat release rate). This broadening could be the result of comparatively lower Froude numbers for NDFs. Further, as expected, the flame temperatures increase with inlet oxygen mole fraction. These trends are supported by Refs. [19] and [39]. Whereas further downstream of the flame tip these temperatures are much larger for earth-gravity normal diffusion flames when compared with microgravity normal diffusion flames.

For inverse diffusion flames, the centreline mixture fraction (fraction of mass contributed by fuel) increases with gravity and oxygen enhancement (Figure 5). The increase in product (CO_2 and H_2O) formation with oxygen-enhancement causes the associated mixture fraction ($= \frac{12}{44}Y_{CO_2} + \frac{2}{18}Y_{H_2O} + Y_{C_2H_6}$) increase. However, no significant change in CO_2 and H_2O mass fraction was observed with gravity variation. The increase in mixture fraction with gravity was caused because of increase in fuel (C_2H_6) mass fraction. Beyond the flame tip the centreline axial velocity, as well as the density, increases for earth-gravity inverse diffusion flames. Hence, the satisfaction of the continuity equation requires that there be an inward radial component of velocity close to the centreline. The radial transfer of fuel associated with this radial velocity is the cause of the larger mixture fraction for earth-gravity inverse diffusion flames when compared with their microgravity counterparts. The above observations indicate that for inverse diffusion flames mixing increases (at least close to the centreline) with gravity and oxygen enhancement.

Since the microgravity normal diffusion flames are wider than earth-gravity normal diffusion flames, they have a larger centreline mixture fraction close to the burner tip. However, further downstream this quantity is smaller in comparison to earth-gravity normal diffusion flames. This is because of their shorter computed flame lengths (Table 2) and smaller downstream axial-velocity.

Species mass fraction and mixture temperature vs. mixture fraction plots from global chemistry computations (Figure 6 for case 1 i.e. 1g_IDF21) verify the correctness of the simplified-state relationships for species mass fractions and mixture temperature presented in the literature [40]. Although, as expected, the species mass fractions show a closely linear dependence upon the mixture fraction, mixture temperature somewhat deviates from this linear relationship. This is attributed to the fact that the original assumptions of constant and equal specific heats for all the species and of zero enthalpies of formation for the product which had been used in the literature for deriving mixture temperature are not valid here. However in general we can conclude that the simplified-state relationships [40] are valid for the fast rate global chemistry model.

Inverse diffusion flames and normal diffusion flames behave differently with gravity-reduction and oxygen enhancement. Inverse diffusion flame lengths and widths increase only slightly with gravity-reduction and oxygen enhancement. Whereas gravity-reduction from 1g to 0 g causes a significant decrease (1.5 to 2 times) in flame length and a significant increase (2 to 3 times) in flame width for normal diffusion flames. Also, oxygen enhancement causes a significant decrease in flame length (about 5 times when going from 21% to 100% O_2) for normal diffusion flames when jet velocity is identical.

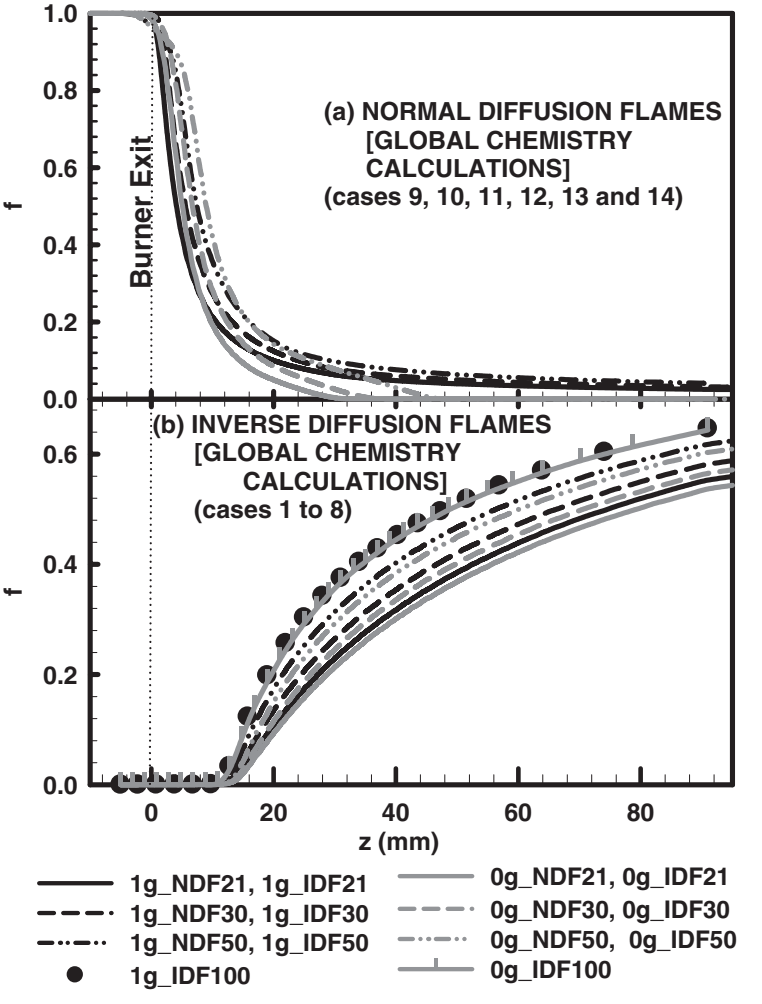

Figure 5. Comparison of mixture fraction at the centreline: (a) Normal Diffusion Flames [cases 9 to 14] and (b) Inverse Diffusion Flames [cases 1 to 8].

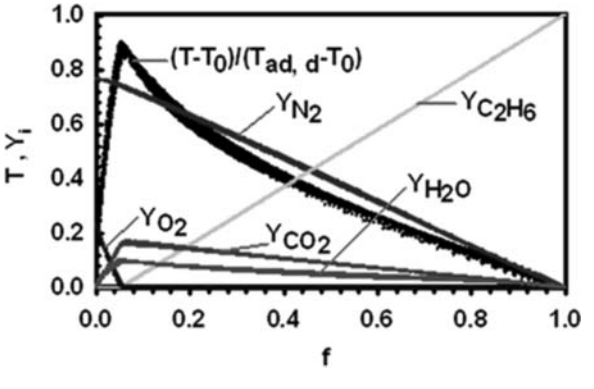

Figure 6. Non-dimensional temperature and species mass fraction distributions as functions of mixture fraction for 1g_IDF21.

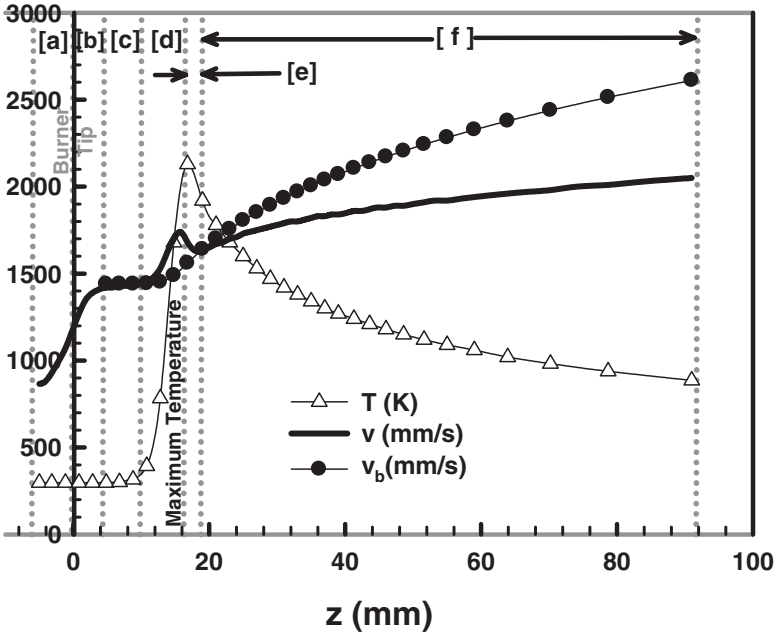

Figure 7. Centreline temperature and axial velocity comparison for 1g_IDF21.

The following sections discuss the centreline as well as radial, species fraction, axial velocity and temperature behaviours for all the 20 cases computed using the global chemistry model. Unless specifically stated, the physical quantities (namely velocity, temperature, forces and mixture fraction) discussed in these sections are along this centreline ($r = 0$).

4.2 *Earth-gravity (1-g) inverse diffusion flames (cases 1, 2, 3 and 4)*

The axial velocity and temperature trends are very similar for these cases. In Figure 7 these two physical quantities are plotted for case 1 (1g_IDF21). In this figure, different zones ([a] through [f]) are identified to facilitate the following discussion. These zones were identified based on the behaviour of the velocity and temperature profiles. Zone [a] represents the region below the burner tip and zone [b] is the region slightly above the burner tip in which the axial-velocity experiences acceleration. In both these zones the temperature remains constant, whereas the axial-velocity shows a sharp rise. The force analysis shows that the fluid experiences an upward axial-pressure force in these zones. The development of the boundary layer on the burner surface causes the deceleration of velocity near this surface. Hence, the satisfaction of the continuity equation leads to the increase in axial-velocity for these two zones. Then there is zone [c] in which the axial-velocity as well as temperature remains constant. Upstream of the flame tip (i.e. the location of peak temperature) in zone [d], this axial-velocity, as well as the temperature, increases sharply. The temperature increase is caused by the combustion heat release. The force plots show that there are upward pressure and buoyant forces in this region. The buoyant force is the result of thermal expansion whereas the appearance of the positive pressure force is not so well understood at this point. Hence it's a combination of pressure force, buoyant force and thermal expansion that causes this velocity to increase in this zone. The axial-velocity beyond this point in zone [e] experiences deceleration. This is the combination of negative pressure and viscous force. Which of these two forces play a dominant role varies from

case to case but in general it is observed that the negative pressure force is the cause of this sharp deceleration. The velocity beyond this point, in zone [f], increases monotonically as expected. This effect is expected because of buoyant acceleration. This effect decreases with downstream distance and the axial-velocity starts to approach uniform profiles.

Figure 7 also shows the centreline axial-velocity contribution due to buoyant force. This is obtained by neglecting viscous and pressure terms in the axial-momentum equation applied at the centreline (r = 0), where there is no radial-velocity component. The assumption of constant pressure, constant molecular mass and applicability of the perfect gas law will lead to the following simplified equation:

$$\frac{\partial (V)^2}{\partial z} = 2\left(\frac{T(K)}{T_0(K)} - 1\right) g \tag{3}$$

Integrating the above equation starting from zone [c] will give us the axial velocity contribution due to buoyant force. The larger value of this velocity than that of the actual computed axial-velocity reveals that the flow at the centreline is primarily dominated by the positive body force.

Radial plots (Figure 8(a, b) for case 1 (1g_IDF21) and case 4 (1g_IDF100)) as well as the centreline plots (Figure 9 for case 1 i.e. 1g_IDF21) reveal that for global chemistry

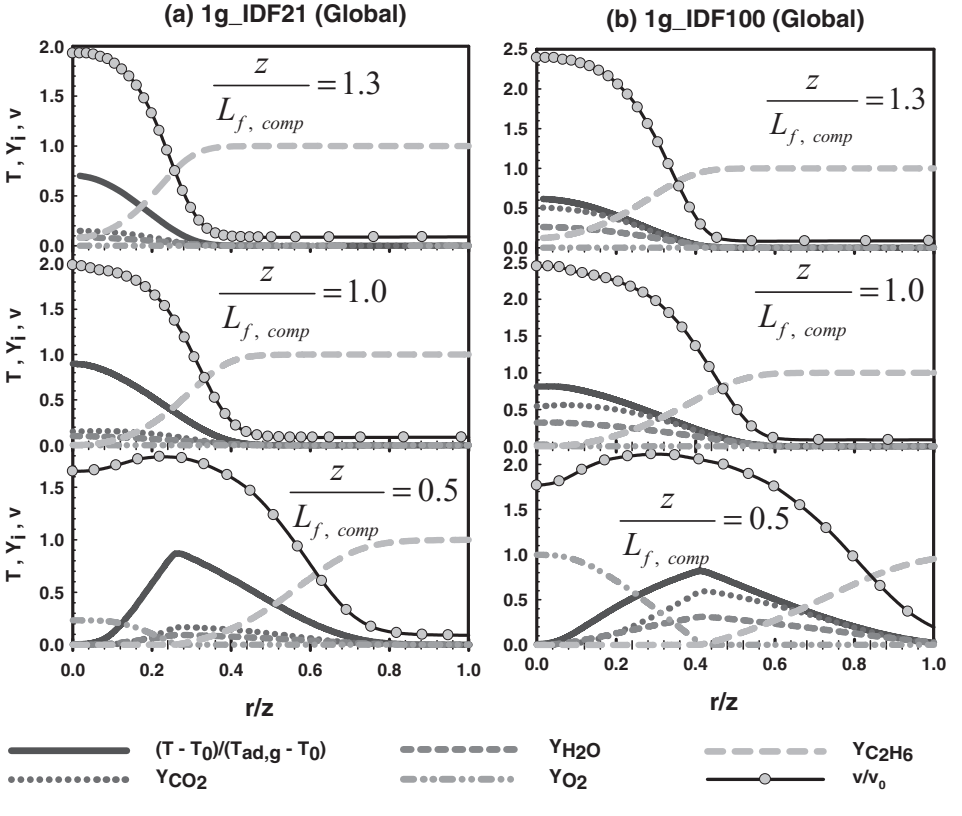

Figure 8. Non-dimensional temperature, axial velocity and species mass fraction distribution at three axial locations for: (a) 1g_IDF21 and (b) 1g_IDF100.

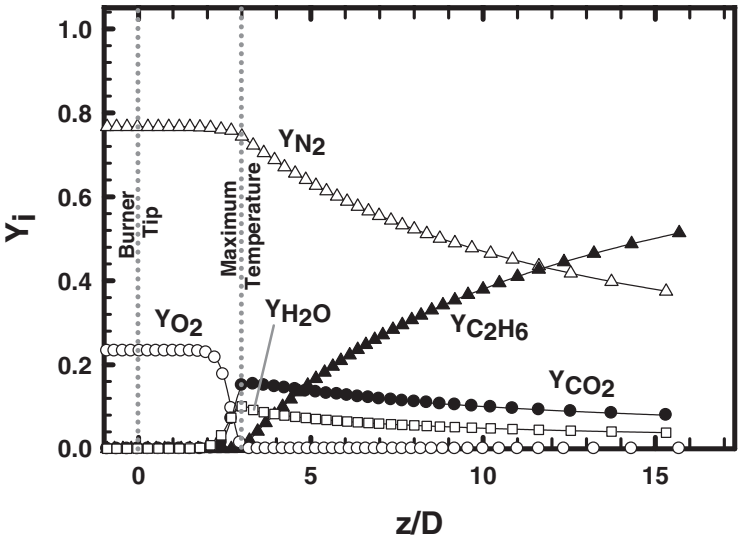

Figure 9. Species mass fraction distribution along the centreline for 1g_IDF21.

computations there is no oxygen or fuel leakage across the flame sheet. The sharp fall in the CO_2 and H_2O concentrations on the oxidisers side of the flame-sheet (a curve joining locations of peak temperatures in radial direction) and their gradual decrease towards the fuel side indicates relatively larger CO_2 and H_2O diffusion into the fuel. It should however be noticed from these plots that, as expected, maximum temperature, maximum CO_2 & H_2O mass fraction and the point where O_2 and fuel are exhausted, occur at identical locations (.i.e. on the flame sheet). As expected, these plots also show that the oxidiser is fully consumed and hence combustion is complete.

4.3 *Microgravity inverse-diffusion computations (cases 5, 6, 7 and 8)*

To facilitate this discussion, Figure 10 shows the centreline axial-velocity and temperature profiles for cases 5, 6 and 7. Till zone [c] these flames behave similarly to earth-gravity inverse diffusion flames. This can be explained based on the fact that for earth-gravity flames body forces come in to play only after zone [c]. In zone [d] there is a sharp increase in the axial velocities due to thermal expansion. After this the velocity monotonically decreases because of shear. Flame lengths and flame widths show a very similar trend to that of earth-gravity inverse diffusion flames. This is because for earth-gravity inverse diffusion flames, the buoyancy effects become significant close to and after the flame tip.

For these flames, the species radial (Figure 11(a, b) for case 5 (0g_IDF21) and case 8 (0g_IDF100)) and the centreline (Figure 12 for case 5 i.e. 0g_IDF21) behaviours are very much similar to their earth-gravity counterparts. The differences observed in their flame-sheet (a curve joining locations of peak temperatures in the radial direction) locations are however because of their different widths and lengths. It is also observed that the high temperature zone in the radial direction becomes broader with gravity reduction (because of the increase in thermal diffusion) and oxygen enhancement (because of the temperature increase).

One difference, worth noticing, between earth-gravity and microgravity inverse diffusion flames is the behaviour of their non-dimensional axial velocity (plots at $\frac{z}{H_f} = 0.5$,

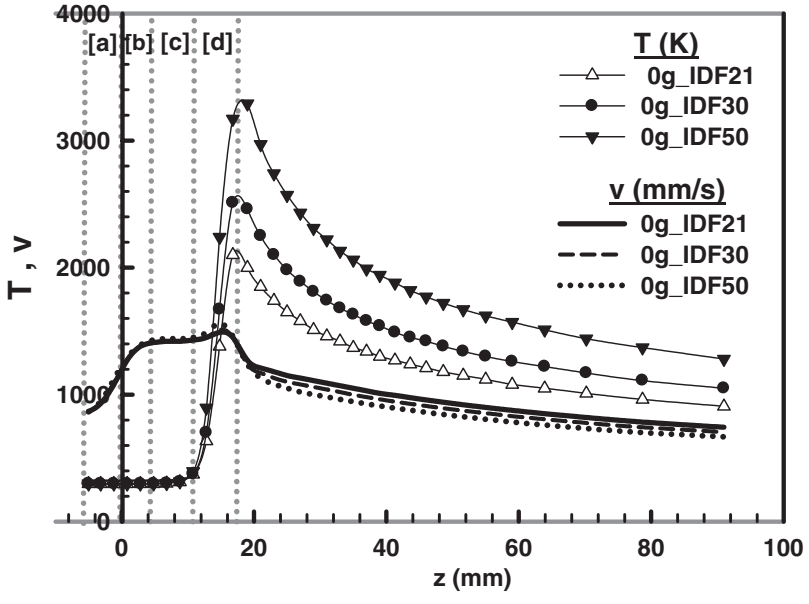

Figure 10. Centreline temperature and axial velocity comparisons for 0g_IDF21, 0g_IDF30, and 0g_IDF50.

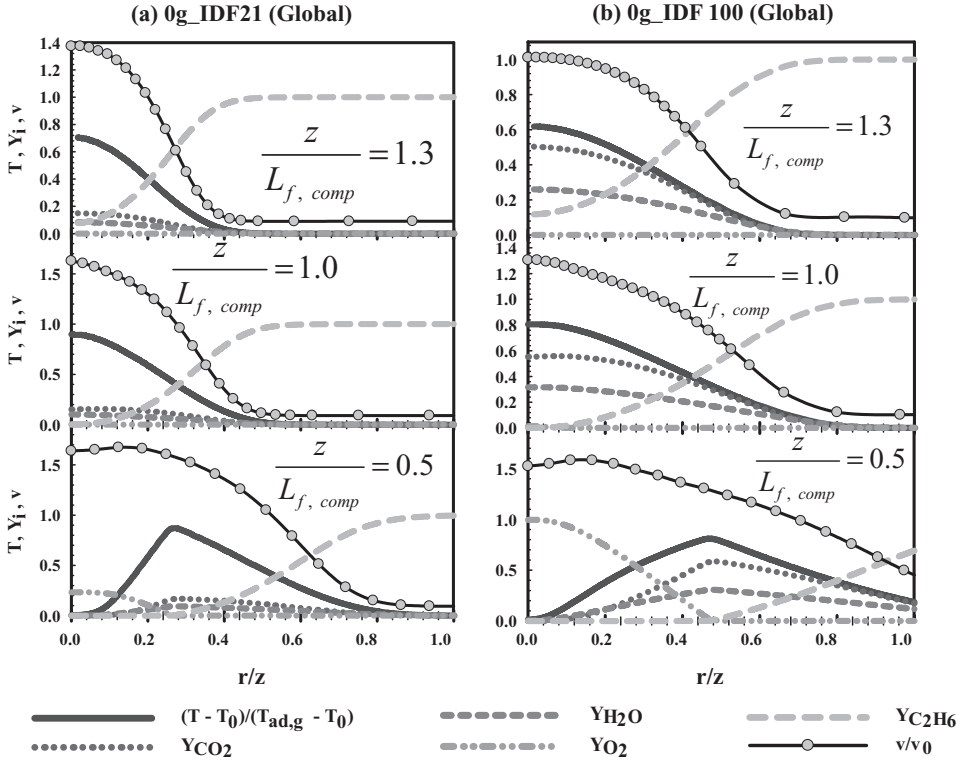

Figure 11. Non-dimensional temperature, axial velocity and species mass fraction distribution at three axial locations for (a) 0g_IDF21 and (b) 0g_IDF100.

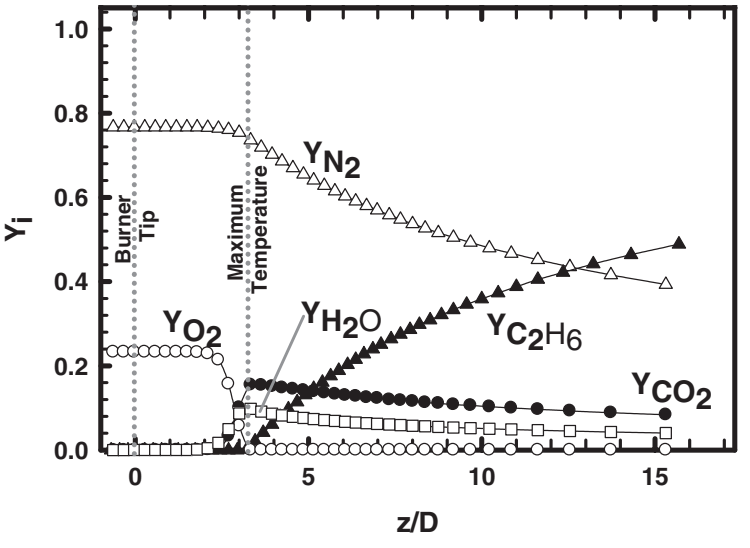

Figure 12. Species mass fraction distribution along the centreline for 0g_IDF21.

Figures 8 and 11). For microgravity flames this velocity nearly monotonically decreases whereas for earth-gravity flames it first accelerates and then decelerates. This acceleration (close to the flame sheet) experienced by the earth-gravity flames is because of buoyancy.

4.4 *Earth-gravity normal diffusion flames (six different cases, cases 9, 10, 11, 15, 16 and 17)*

Cases 9, 10 and 11 are chosen in such a manner that their heat release rates are identical to their inverse diffusion counterparts (i.e. cases 1, 2 and 3). This is done so that we can compare inverse and normal diffusion flames. Cases 9, 15, 16 and 17 are chosen in such a manner that all other parameters except oxygen content are identical. These cases are so chosen for the purpose of studying the effect of oxygen enhancement.

Figure 13 shows the centreline axial-velocity and temperature profiles for case 9 (1g_NDF21), which are similar to the other five cases. Note that these flames are low Froude number flames (Table 1) compared to the inverse diffusion flames. Therefore, the thermal diffusion effects from the tip of the flame reach closer to the burner causing an earlier temperature rise along the axial direction. The force calculations show that the initial sharp acceleration of the axial-velocities before the flame tip is because of buoyancy. However, because of the fall in temperature, this buoyant force decreases as we go downstream. The axial-velocity contribution due to buoyant force (calculated by integrating Equation (3), beginning from $z = -5$ mm) again reveal that the buoyant forces play a dominant role. This is also supported by the large magnitude of the computed buoyant forces.

Just as for inverse diffusion flames, for these flames also the radial plots (Figure 14(a, b) for case 9 (1g_NDF21) and case 11 (1g_NDF50)) as well as the centreline plots (Figure 15 for case 9 i.e. 1g_NDF21) reveal that there is no oxygen or fuel leakage across the flame sheet, there is a sharp fall in the CO_2 and H_2O concentrations on the oxidisers side of the flame sheet, and the combustion is complete. Also, as expected, maximum temperature, maximum CO_2 & H_2O mass fraction and the point where O_2 and fuel are exhausted, occur at

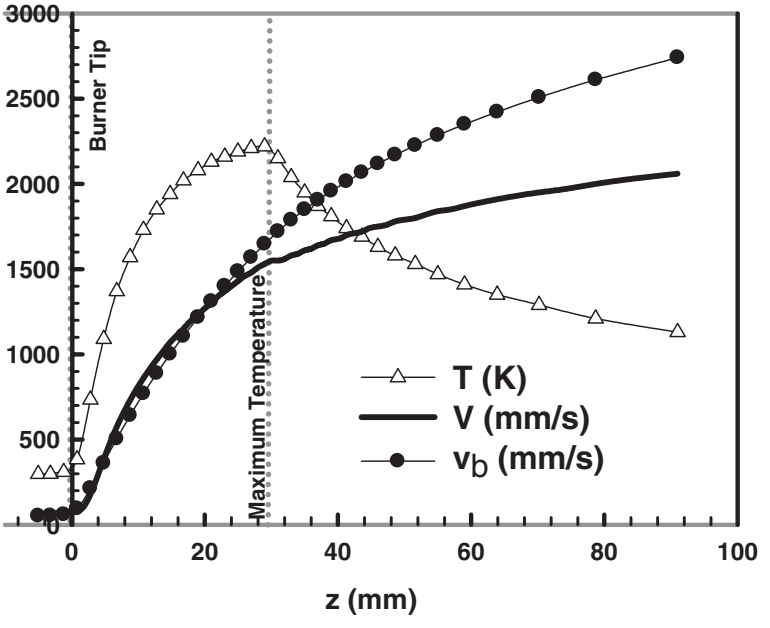

Figure 13. Centreline temperature and axial velocity comparison for 1g_NDF21 [case 9].

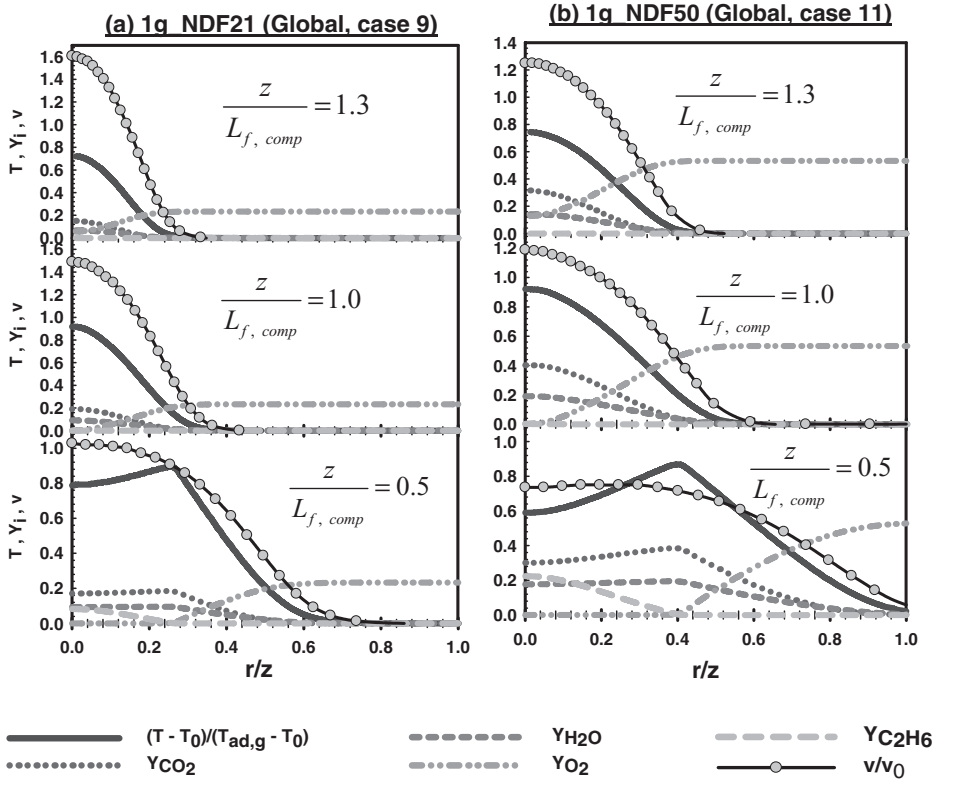

Figure 14. Non-dimensional temperature, axial velocity and species mass fraction distribution at three axial locations for: (a) 1g_NDF21 [case 9] and (b) 1g_NDF50 [case 11].

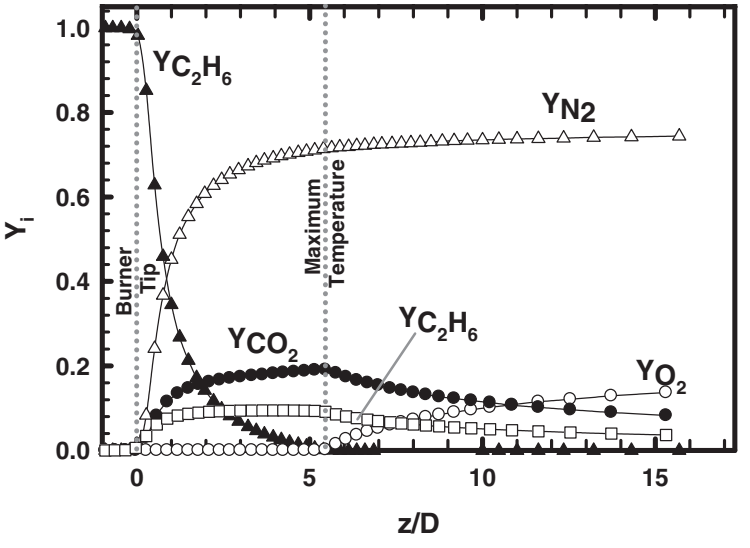

Figure 15. Species mass fraction distribution along the centreline for 1g_NDF21 [case 9].

identical locations (i.e. on the flame sheet). We also observe (Figure 14(a, b)) that; thermal, species and momentum transfers in radial direction increase with oxygen enhancement.

4.5 *Microgravity normal diffusion flames (cases 12, 13, 14, 18, 19 and 20)*

Cases 12, 13, and 14 are chosen in such a manner that their heat release rates are identical to their inverse diffusion counterparts (i.e. cases 5, 6 and 7). This is done so that we can

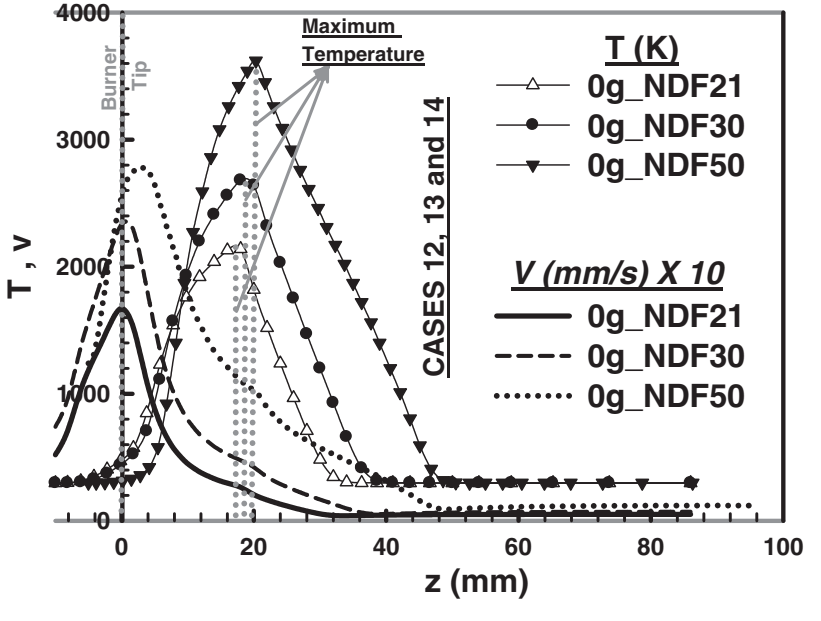

Figure 16. Centreline temperature and axial velocity comparisons for 0g_NDF21, 0g_NDF30, and 0g_NDF50 (cases 12, 13 and 14 respectively).

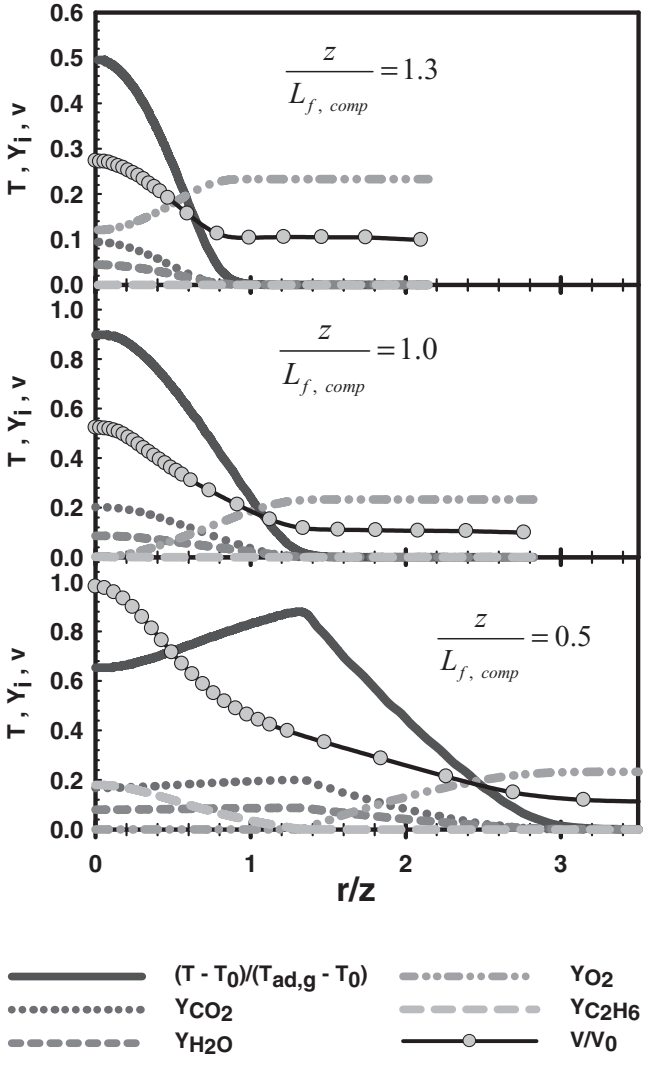

Figure 17. Non-dimensional temperature, axial velocity and species mass fraction distribution at three axial locations for 0g_NDF21 [case 12].

compare inverse and normal diffusion flames. Cases 12, 18, 19 and 20 are chosen in such a manner that all other parameters except oxygen content are identical. These cases are so chosen for the purpose of studying the effect of oxygen enhancement.

Figure 16 shows the centreline axial-velocity and temperature profiles for cases 12, 13 and 14. Just as for earth-gravity normal diffusion flames the jet velocities are relatively smaller, hence thermal diffusion causes the temperature rise to occur earlier (just above the burner tip). However for these microgravity flames, after the burner tip the axial velocity experiences deceleration mainly because of shear. We observe that upstream of the burner tip these flames experience larger acceleration when compared with their earth-gravity counter parts (i.e. cases 9, 10 and 11). Since the axial velocities decrease beyond the burner

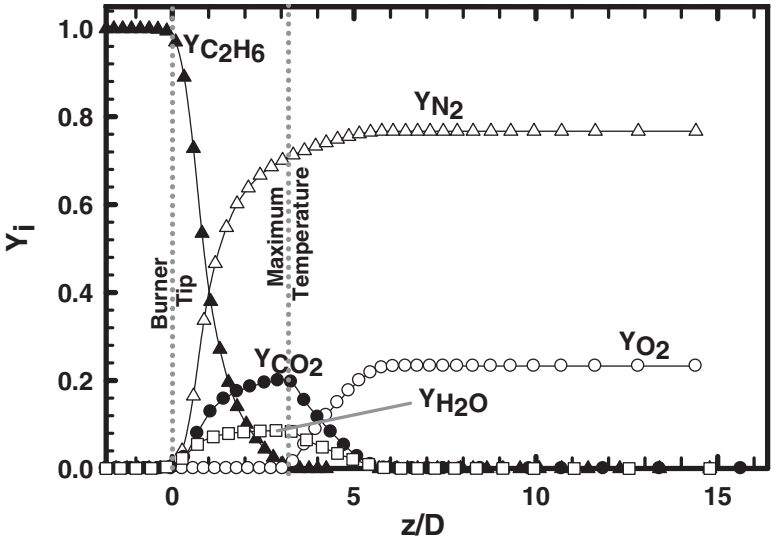

Figure 18. Species mass fraction distribution along the centreline for 0g_NDF21 [case 12].

tip and their magnitude in general is small, they have to gather enough momentum before the burner tip for this inertia to last to the flame tip and beyond.

These flames are observed to be spherical in shape and are two to three times wider in comparison to earth-gravity diffusion flames (Table 2). In addition they are shorter in length and the flame sheet goes below the burner tip (for example the flame-sheet goes 4.5 mm, 3.8 mm and 1.5 mm below the burner tip for cases 12, 13 and 14, respectively). All these effects decrease with the increase in jet velocity. All these indicate that because of low velocities, diffusion plays a dominant role in these flames.

For these flames, the species radial (Figure 17 for case 12 i.e. 0g_NDF21) and the centreline (Figure 18 for case 12 i.e. 0g_NDF21) behaviours are very much similar to their earth-gravity counterparts. The differences observed in their flame sheet locations are however because of their different widths and lengths. One difference, worth noticing, between earth-gravity and microgravity normal diffusion flames is that for microgravity normal diffusion flames the centreline CO_2 and H_2O mass fraction eventually becomes negligible, whereas for the given computational domain's length, this was not observed for earth-gravity normal diffusion flames. The centreline axial velocities, being relatively very large for earth-gravity flames, do not give sufficient time for these species to diffuse. However the centreline axial velocities eventually become negligible for microgravity flames and hence these species diffuse sufficiently for their local mass fraction to become negligible. Just as for inverse diffusion flames, it was also observed for these flames that the high temperature zone in the radial direction becomes broader with gravity reduction (because of the increase in thermal diffusion). Since these flames are low Froude number flames the diffusive effect is much more pronounced for them.

5. Conclusions

Global chemistry calculations were performed for ethane fuelled laminar gas jet diffusion flames, emphasising the effects of oxygen enhancement, gravity, and inverse burning

on species mass fraction, axial velocity and temperature. The mole fraction of oxygen in the oxidiser was varied from 0.21−1.0. Qualitative comparisons were made with the experimental results [4]. The major findings were:

1. Oxygen enhanced conditions resulted in increased flame temperatures. This resulted in increased buoyancy effects for the earth-gravity flames. Additionally, because of the presence of buoyant force for earth-gravity flames, their centreline axial velocities continue to increase after the flame tip whereas beyond the flame tip these velocities slowly decrease for all microgravity flames.
2. When compared with inverse diffusion flames, the flame shape and size changes with gravity-variation and oxygen enhancement are much more pronounced for normal diffusion flames. As a result, for IDFs, gravity had relatively smaller influences on the flame temperatures.
3. Computations confirmed the dominance of radial diffusion in the absence of gravity for the NDFs. The increase in flame width, by two to three times, and the attachment of the flame sheet below the burner tip observed for the normal diffusion flames in microgravity support this conclusion.

Acknowledgements

This work was supported by NASA's Office of Biological and Physical Processes under the management of Merrill King. Thanks to Dr. Dave Seaman, Dr. Bill Whitson and Dr. Chinh Le for helping in facilitating computations.

References

[1] C.E. Baukal, in *Oxygen-Enhanced Combustion*, C.E. Baukal, ed., CRC Press, Boca Raton, FL, 1998.
[2] B. Burrough, *Dragonfly: NASA and the Crisis aboard Mir*, Harper Collins, New York, 1998, pp. 123–132.
[3] H.D. Ross, *in Microgravity Combustion*, in *Basics of Microgravity Combustion*, H.D. Ross, ed., Academic Press, San Diego, 2001, pp. 1–34.
[4] P.B. Sunderland, S.S Krishnan and J.P. Gore, *Effects of oxygen enhancement and gravity on normal and inverse laminar jet diffusion flames*, Combust. Flame 136 (2004), pp. 254–256.
[5] R.B. Edelman, O.F. Fortune, G. Weilerstein, T.H. Cochran and J.B. Haggard, *An analytical and experimental investigation of gravity effects upon laminar gas jet diffusion flames*, Proc. Combust.Inst. 14 (1972), pp. 399–412.
[6] P.B. Sunderland, B.J. Mendelson, Z.G. Yuan and D.L. Urban, *Shapes of buoyant and nonbuoyant laminar jet diffusion flames*, Combust. Flame 116 (1999), pp. 376–385.
[7] M.Y. Bahadori, R.B. Edelman, D.P. Stocker and S.L. Olson, *Ignition and behavior of laminar gas-jet diffusion flames in microgravity*, AIAA J. 28 (1990), pp. 236–244.
[8] M.Y. Bahadori, D.P. Stocker, D.F. Vaughan, L. Zhou and R.B. Edelman, *Effects of Buoyancy on Laminar, Transitional and Turbulent Gas Jet Diffusion Flames,* in *Modern Developments in Energy, Combustion and Spectroscopy*, F.A. Williams, A.K. Oppenheim, D.B. Olfe, and M. Lapp, eds., Pergamon Press, Oxford, 1993, pp. 49–66.
[9] P.B. Sunderland, R.L. Axelbaum, D.L. Urban, B.H. Chao and S. Liu, *Effects of structure and hydrodynamics on the sooting behavior of spherical microgravity diffusion flames*. Combust. Flame 132 (2003), pp. 25–33.
[10] P. Van-Hulle, M. Talbaut, M. Weill and A. Coppalle, *Inversion method and experiment to determine the soot refractive index: Application to turbulent diffusion flames*, Meas. Sci. Technol. 13 (2002), pp. 375–382.
[11] L.G. Blevins, G.W. Mulholland, B.A., Jr. Benner, R.A. Fletcher and E.B. Steel, *Composition and shape of early soot collected from inverse flames*, presented at the Fall Technical Meeting of the Western States Section of The Combustion Institute, Salt Lake City, UT, 2001.

[12] C.R. Shaddix, T.C. Williams, L.G. Blevins and R.W. Schefer, *Flame structure of steady and pulsed sooting inverse jet diffusion flames*, Proc. Combust. Inst. 30 (2005), pp. 1501–1508.

[13] D.L. Urban, Z.-G. Yuan, P.B. Sunderland, G.T. Linteris, J.E. Voss, K.-C. Lin, Z. Dai, K. Sun and G.M. Faeth, *Structure and soot properties of nonbuoyant ethylene/air laminar jet diffusion flames*, AIAA J. 36 (1998), pp. 1346–1360.

[14] K.-C. Lin, G.M. Faeth, P.B. Sunderland, D.L. Urban and Z.-G. Yuan, Shapes of nonbuoyant round luminous hydrocarbon/air laminar jet diffusion flames, Combust. Flame 116 (1999), pp. 415–431.

[15] S.S. Hwang and J.P. Gore, *Radiation heat transfer and characteristics of oxygen enriched double inverse diffusion flame*, presented at The Second Joint Meeting of the US States Section of The Combustion Institute, Oakland, CA, 2001.

[16] K.T. Walsh, J. Fielding, M.D. Smooke, M.B. Long and A. Liñán, *A comparison of computational and experimental lift-off heights of coflow laminar diffusion flames*, Proc. Combust. Inst. 30 (2005), pp. 357–365.

[17] V.R. Katta, L.P. Goss and W.M. Roquemore, *Effect of nonunity Lewis number and finite rate chemistry on the dynamics of a hydrogen air jet diffusion flame*, Combust. Flame 96 (1994), pp. 60–74.

[18] W.M. Roquemore and V.R. Katta, *Role of flow visualization in the development of UNICORN*, J. Visualization 2 (2000), pp. 257–272.

[19] V.R. Katta, L.G. Blevins and W.M. Roquemore, *PAH formation in an inverse diffusion flame,* 41st Aerospace Sciences Meeting, AIAA-2003-0666, 2003.

[20] Z. Shu, S.K. Aggarwal, V.R. Katta and I.K. Puri, *A numerical investigation of the flame structure of an unsteady inverse partially premixed flame*, Combust. Flame 111 (1997), pp. 296–311.

[21] Z. Shu, S.K. Aggarwal, V.R. Katta and I.K. Puri, *Flame vortex dynamics in an inverse partially premixed combustor: The Froude number effects*, Combust. Flame 111 (1997), pp. 276–286

[22] N. Smith, J. Gore, J. Kim and Q. Tang, *Radiation models*, International Workshop on Measurement and Computation of Turbulent Nonpremixed Flames, 2001. Available at http://www.ca.sandia.gov/tdf/Workshop/Submodels.html.

[23] V.R. Katta, L.P. Goss and W.M. Roquemore, *Numerical investigations of transitional H_2/N_2 jet diffusion flames*, AIAA J. 32 (1994), pp. 84–94.

[24] V.R. Katta, L.P. Goss and W.M. Roquemore, *Simulation of vertical structures in a jet diffusion flame*, Int. J. Numer. Methods Heat Fluid Flow 4 (1994), pp. 413–424.

[25] V.R. Katta, C.D. Carter, G.J. Fiechtner, W.M. Roquemore, J.R. Gord and J.C. Rolon, *Interaction of a vortex with a flat flame formed between opposing jets of hydrogen and air*, Proc. Combust. Inst. 27 (1998), pp. 587–594.

[26] X. Qin, I.K. Puri, S.K. Aggarwal and V.R. Katta, *Gravity, radiation and coflow effects on partially premixed flames*, Phys. Fluids 6 (2004), pp. 2963–2974.

[27] G.W. Sidebotham and I. Glassman, *Flame temperature, fuel structure, and fuel concentration effects on soot formation in inverse diffusion flames*, Combust. Flame 90 (1992), pp. 269–283.

[28] C.R. Kaplan and K. Kailasanath, *Flow-field effects on soot formation in normal and inverse methane–air diffusion flames*, Combust. Flame 124 (2001), pp. 275–294.

[29] L. Blevins, R. Fletcher, B. Benner, E. Steel and G. Mulholland, The existence of young soot in the exhaust of inverse diffusion flames, Proc. Combust. Inst. 29 (2003), pp. 2325–2333.

[30] F. Xu, Z. Dai and G.M. Faeth, Flame and soot boundaries of laminar jet diffusion flames, AIAA J. 40 (2002), pp. 243–2446.

[31] K.N. Al-Ammar, A.K. Agrawal and S.R. Gollahalli, *Quantitative measurements of laminar hydrogen gas-jet diffusion flames in a 2.2 s drop tower*, Proc. Combust. Inst. 28 (2000), pp. 1997–2000.

[32] P.S. Greenberg and J.C. Ku, *Soot volume fractions in normal and reduced gravity laminar acetylene diffusion flames*, Combust. Flame 108 (1997), pp. 227–230.

[33] H. Wang and M. Frenklach, *A detailed kinetic modeling study of aromatics formation in laminar premixed acetylene and ethylene flames*, Combust. Flame 110 (1997), pp. 173–221.

[34] H. Guo, F. Liu and J. Smallwood, *Soot and NO formation in counterflow ethylene/oxygen/nitrogen diffusion flames*, Combust. Theor. Model. 8 (2004), pp. 475–489.

[35] R. Siegel and J.R. Howell, *Thermal Radiation Heat Transfer*, Hemisphere, New York, 1981.

[36] M.D. Smooke, C.S. McEnally, L.D. Pfefferle, R.J. Hall and M.B. Colket, *Computational and experimental study of soot formation in a co-flow, laminar diffusion flame*, Combust. Flame 117 (1999), pp. 117–139.

[37] F.A. Williams, *Combustion Theory - The Fundamentals of Chemically Reacting Flow systems*, Appendix E, Addison-Wesley Publishing Co., Reading, MA, 1985.
[38] B.P. Leonard, *A stable and accurate convective modeling procedure based on quadratic upstream interpolation*, Comput. Meth. Appl. Mech. Eng. 19 (1979), pp. 59–98.
[39] M.Y. Bahadori, D.P. Stocker and U. Hegde, *Radiative loss from non-premixed flames in reduced-gravity environments*, Combust. Sci. Technol. 167 (2002), pp. 169–186.
[40] S.R. Turns, *An Introduction to Combustion: Concepts and Applications*, McGraw-Hill, Singapore, 2000.